A Dual-Modality Linker Enables Site-Specific Conjugation of Antibody Fragments for ^{18}F-Immuno-PET and Fluorescence Imaging

Kirstin A. Zettlitz*, Christopher M. Waldmann*, Wen-Ting K. Tsai, Richard Tavaré, Jeffrey Collins, Jennifer M. Murphy, and Anna M. Wu

Crump Institute for Molecular Imaging, Department of Molecular and Medical Pharmacology, David Geffen School of Medicine at UCLA, Los Angeles, California

Antibody-based dual-modality (PET/fluorescence) imaging enables both presurgery antigen-specific immuno-PET for noninvasive whole-body evaluation and intraoperative fluorescence for visualization of superficial tissue layers for image-guided surgery. **Methods:** We developed a universal dual-modality linker (DML) that facilitates site-specific conjugation to a cysteine residue–bearing antibody fragment, introduction of a commercially available fluorescent dye (via an amine-reactive prosthetic group), and rapid and efficient radiolabeling via click chemistry with ^{18}F-labeled *trans*-cyclooctene (^{18}F-TCO). To generate a dual-modality antibody fragment–based imaging agent, the DML was labeled with the far-red dye sulfonate cyanine 5 (sCy5), site-specifically conjugated to the C-terminal cysteine of the anti-prostate stem cell antigen (PSCA) cys-diabody A2, and subsequently radiolabeled by click chemistry with ^{18}F-TCO. The new imaging probe was evaluated in a human PSCA-positive prostate cancer xenograft model by sequential immuno-PET and optical imaging. Uptake in target tissues was confirmed by ex vivo biodistribution. **Results:** We successfully synthesized a DML for conjugation of a fluorescent dye and ^{18}F. The anti-PSCA cys-diabody A2 was site-specifically conjugated with either DML or sCy5 and radiolabeled via click chemistry with ^{18}F-TCO. Immuno-PET imaging confirmed in vivo antigen-specific targeting of prostate cancer xenografts as early as 1 h after injection. Rapid renal clearance of the 50-kDa antibody fragment enables same-day imaging. Optical imaging showed antigen-specific fluorescent signal in PSCA-positive xenografts and high contrast to surrounding tissue and PSCA-negative xenografts. **Conclusion:** The DML enables site-specific conjugation away from the antigen-binding site of antibody fragments, with a controlled linker-to-protein ratio, and combines signaling moieties for 2 imaging systems into 1 molecule. Dual-modality imaging could provide both noninvasive whole-body imaging with organ-level biodistribution and fluorescence image–guided identification of tumor margins during surgery.

Key Words: immuno-PET; fluorescence image-guided surgery (FIGS); cys-diabody; ^{18}F; click chemistry

J Nucl Med 2019; 60:1467–1473
DOI: 10.2967/jnumed.118.223560

Although a variety of molecular imaging modalities is available, no single one provides overall structural, functional, and molecular information. Combining 2 signaling moieties in 1 molecule can provide complementary imaging applications; therefore, targeted multimodality imaging and theranostics approaches are becoming more popular (*1*). Ideally, dual-modality imaging would facilitate whole-body imaging for staging and surgical planning, as well as real-time imaging for guided surgery, and could improve patient outcomes, especially in cancers with curative surgery as the primary treatment option (e.g., prostate or pancreatic cancer) (*2,3*). One promising combination is dual-modality PET and fluorescence imaging, which enables a preoperative whole-body evaluation of tumor location and burden and fluorescence imaging guidance to identify positive tumor margins or local metastases (fluorescence image–guided surgery).

Targeted dual-modality imaging requires selecting a favorable combination of radionuclide and fluorescent dye, an antigen-specific targeting moiety with suitable pharmacokinetics for imaging, and a conjugation technique that results in a predictable and consistent product (*1,4*).

Monoclonal antibodies show high antigen specificity and affinity, making them valuable targeting vectors both for imaging and for therapy. IgGs contain numerous reactive amino acids available for conjugation to chelators or radionuclides and fluorescent dyes, and a variety of therapeutic monoclonal antibodies against tumor targets (e.g., epidermal growth factor receptor, human epidermal growth factor receptor 2, CD20, epithelial cellular adhesion molecule, and prostate-specific membrane antigen) have been studied as dual-modality imaging agents for preclinical imaging (*1,5*). Major disadvantages of using full-length IgGs for imaging are the long half-life, delaying imaging (4–6 d after injection), and unwanted biologic effects mediated by the Fc portion.

However, antibodies can be engineered into smaller fragments with optimized pharmacokinetics, such as diabodies (scFv dimer, ~50 kDa) that exhibit rapid localization to antigen-expressing tumor tissue (peak uptake, 1–2 h after injection) and sufficient clearance from normal tissues and blood pool (half-life, 2–5 h in

Received Nov. 20, 2018; revision accepted Mar. 6, 2019.
For correspondence or reprints contact: Kirstin A. Zettlitz, Department of Molecular Imaging and Therapy, Beckman Research Institute at City of Hope, 1500 E. Duarte Rd., Duarte, CA 91010.
E-mail: kzettlitz@coh.org
*Contributed equally to this work.
Published online Mar. 15, 2019.

mice) to facilitate high-contrast imaging within a few hours after tracer injection (*6*). Removal of the Fc domain eliminates interaction with the immune system and FcRn recycling, resulting in biologic inertness. Diabodies can be further engineered to contain C-terminal cysteine residues (cys-diabody, cDb) that enable site-specific conjugation opposite from the antigen-binding site through thiol-reactive groups (*7*). Site-specific labeling results in more homogeneous and better defined constructs, prevents interference with antigen binding, and allows a precisely controlled load-to-protein ratio (*8*).

Fluorescence image guidance during surgery has become available for clinical trials because of specialized intraoperative imaging systems with acquisition times that enable real-time imaging (*9,10*). Most antibody-based probes in clinical trials use near-infrared fluorescent dyes (~700–1,000 nm), such as IRDye800CW, because tissue exhibits almost no autofluorescence in the near-infrared fluorescent spectrum and near-infrared fluorescent light can be detected at a tissue depth of millimeters (*11*).

We have previously targeted the anti-prostate stem cell antigen (PSCA) for dual-modality imaging of prostate and pancreatic cancer by conjugating the cys-minibody A11cMb and the cDb A2 (A2cDb) with near-infrared fluorescent dyes (Cy5.5 or IRDye800CW, site-specifically) and ^{124}I or ^{89}Zr (random labeling to tyrosine or lysine residues, respectively) (*12,13*). However, we believe that the antibody fragment–based dual-modality imaging approach can be improved by choosing a more favorable fluorescent dye, positron emitter, and conjugation method.

The far-red dye sulfonate cyanine 5 (sCy5; excitation, 646 nm; emission, 662 nm) offers an attractive alternative to IRDye800CW for conjugation to smaller antibody fragments, adding less molecular weight (~780 Da) and less charge (net charge, −1) and allowing conjugation in aqueous solutions. The high absorption coefficient and reasonable quantum yield (0.27) result in excellent brightness. Furthermore, cyanine-based dyes are residualizing, and the significant retention in cells (several days) extends the detection window for the fluorescent signal (*14,15*).

The fast pharmacokinetics of the cDb format align with the half-life of ^{18}F (half-life, 110 min), which offers excellent imaging properties (97% positron emission or β^+ decay, mean positron range of 0.6 mm). Because ^{18}F is widely available and ^{18}F-FDG is commonly used, clinicians are accustomed to both acquisition and interpretation of ^{18}F-FDG PET scans, and transitioning toward ^{18}F-labeled diabody scans should be straightforward.

The conjugation of short-lived radionuclides is complicated by elaborate procedures under time constraints and conditions that might damage the protein or the fluorescent dye. Rapid bioorthogonal reactions with high second-order rate constants (click chemistry) could overcome these challenges for ^{18}F-labeling of proteins (*16*). The inverse electron demand [4 + 2] Diels-Alder (IEDDA) reaction between 1,2,4,5-tetrazines and *trans*-cyclooctene (TCO) is an extremely rapid cycloaddition, proceeds without a catalyst, and is effective under mild conditions (neutral pH, room temperature) (*17,18*).

We developed a universal multifunctional dual-modality linker (DML) to enable site-specific conjugation to engineered cysteine residues, conjugation of fluorescent dyes via amine-reactive groups and rapid ^{18}F-labeling via click chemistry. To generate a dual-modality antibody-based imaging agent, the DML was labeled with sCy5, site-specifically conjugated to the C-terminal cysteine of A2cDb, and subsequently radiolabeled by click chemistry with ^{18}F-TCO. The new imaging probe (^{18}F-DMLsCy5-A2cDb) was evaluated in a human PSCA-positive prostate cancer xenograft model by sequential immuno-PET and optical imaging.

MATERIALS AND METHODS

DML Synthesis

A detailed description of the linker synthesis can be found in the supplemental materials (available at http://jnm.snmjournals.org). In short, the linker scaffold was prepared by conjugation of mal-amido-PEG_2-*N*-hydroxysuccinimide (NHS) (Broadpharm) with *N*-α-*tert*-butyloxycarbonyl-L-lysine (Combi-Blocks). Subsequent introduction of an amino-functionalized tetrazine moiety via peptide coupling, removal of the *tert*-butyloxycarbonyl protecting group from L-lysine, and coupling of the amine-reactive sulfo-cyanine5 NHS ester (Lumiprobe) concluded the synthesis of DML-sCy5. The purity was assessed by high-performance liquid chromatography and the identity confirmed by electrospray ionization–mass spectrometry.

Site-Specific Conjugation of the DML to A2cDb

Generation and production of the anti-PSCA cDb 2B3 A2 (A2cDb) were previously described (*19,20*). DML or DML-sCy5 (a 3- to 5-fold molar excess) was incubated with reduced (tris(2-carboxyethyl)phosphine, 1 h, 22°C) A2cDb (100 μg/50 μL) for 2 h at room temperature or overnight at 4°C. Conjugates were separated from excess linker using Micro Bio-Spin size-exclusion columns (BioRad) preblocked with phosphate-buffered saline and 1% fetal bovine serum. Dye-to-protein (D/P) ratio was determined by measuring protein (280 nm) and dye (650 nm, correction factor of 0.04) concentration on a NanoDrop 2000 (Thermo Fisher Scientific).

Conjugates were analyzed by sodium dodecyl sulfate–polyacrylamide gel electrophoresis and by size-exclusion chromatography using a Superdex-75 HR10/30 column in an Äkta purifier (GE Healthcare).

Binding to human PSCA-expressing prostate cancer cells (22Rv1-PSCA) was analyzed by flow cytometry (*21*). Cells were incubated with serial dilutions of A2cDb-DMLsCy5 for 2 h at 4°C and, after washing, were analyzed using an LSRFortessa X-20 Sorp (BD Biosciences). Data were analyzed using FlowJo (version 9.3.2) and were fitted to a 1-site-saturation binding model in Prism 7 (GraphPad Software, Inc.). The apparent affinity was calculated from 3 independent binding curves.

Radiosynthesis of ^{18}F-TCO and Radiolabeling of A2cDb-DML by Click Chemistry

^{18}F-TCO was synthesized using the Elixys Flex/Chem automated radiochemical synthesizer (Sofie Biosciences) and eluted in dimethyl sulfoxide:0.5% sodium-ascorbate solution 1:1 (v/v) as previously described (*22*). More details can be found in the supplemental materials (*22–24*).

^{18}F-TCO (37–111 MBq) was added to A2cDb-DML or A2cDb-DMLsCy5 (100–300 μg in phosphate-buffered saline) to a final dimethyl sulfoxide concentration of 10% and incubated at room temperature for 10 min. Labeling efficiency was determined by instant thin-layer chromatography (instant thin-layer chromatography strips for monoclonal antibody preparation; Biodex Medical Systems) with acetonitrile as the solvent and γ-counted in a Wizard 3′ 1480 automatic γ-counter (Perkin Elmer). Radiolabeled antibody fragments were purified using Micro Bio-Spin columns, and radiochemical purity was determined by instant thin-layer chromatography as described above. The immunoreactive fraction was determined by incubating a trace amount (<0.5 pmol) of ^{18}F-DML-A2cDb with excess antigen-expressing cells (22Rv1-PSCA) for 1 h at room temperature and γ-counting supernatant versus cell-bound activity.

Prostate Cancer Xenograft Mouse Model (22Rv1-PSCA)

All procedures performed involving animals were approved by the UCLA Chancellor's Animal Research Committee.

Cell lines 22Rv1 and 22Rv1-PSCA were cultured in RPMI1640 and 10% fetal bovine serum (*21*), and tumors were inoculated subcutaneously

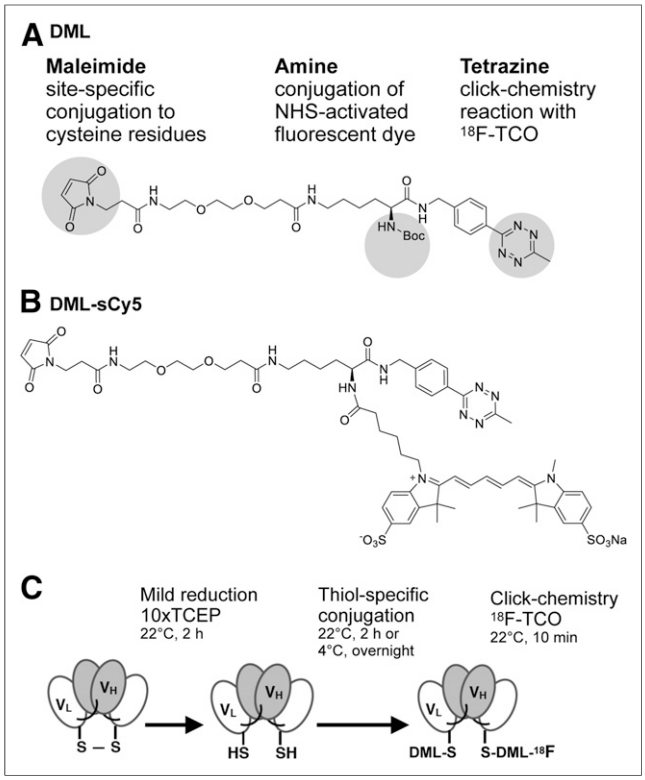

FIGURE 1. Concept: DML. (A) Structure of DML containing 3 functional groups. (B) Sulfo-cyanine5 NHS ester was conjugated to amine group (DML-sCy5). (C) Schematic of site-specific conjugation and radiolabeling. Reducing A2cDb C-terminal disulfide-bridge presents thiol groups for conjugation with maleimide group. Radiofluorination is achieved by click chemistry using ^{18}F-TCO. TCEP = tris(2-carboxyethyl)phosphine; V_H = heavy-chain variable domain; V_L = light-chain variable domain.

(1×10^6 cells/100 μL in 1:1 phosphate-buffered saline:Matrigel [BD Biosciences]) in the shoulder of male nude mice (8–12 wk, ~25 g, JAX002019; Jackson Laboratories) as previously described (*13*).

Immuno-PET/CT and Near-Infrared Fluorescence Imaging

Approximately 10 μg (3–4.8 MBq) of ^{18}F-DML-A2cDb or ^{18}F-DMLsCy5-A2cDb were injected into the tail vein of tumor-bearing mice (3–4 mice/group, $n = 2$). Mice were anesthetized with 1.5% isoflurane, and small-animal PET scans (Inveon; Siemens) were acquired for 60 min (dynamic scan), followed by static 10-min scans at 2 and 4 h after injection. Images were reconstructed using ordered-subsets expectation maximization maximum a posteriori algorithms, overlaid with CT scans (CrumpCAT; UCLA in-house small-animal scanner), and shown as whole-body maximum-intensity projections.

Optical imaging was conducted postmortem with the skin removed or of dissected tumors and organs ex vivo using the IVIS Lumina II system (PerkinElmer) with 675-nm excitation/694-nm emission (Cy5.5) and 5-s exposure time. Living Image Software (IVIS Imaging Systems; PerkinElmer) was used to display fluorescent/visible light overlays.

Region-of-Interest (ROI) Analysis and Ex Vivo Biodistribution

PET images were analyzed using AMIDE (*25*). For quantitative ROI analysis, the mean voxel value was converted to percentage injected dose per gram (%ID/g, assuming a tissue density of 1 g/mL) using the decay-corrected injected dose and empirically determined cylinder factor for ^{18}F in the Inveon PET scanner. Partial-volume correction was not applied, because of the complexity of organ shape, volume, and proximity to organs with high activity.

Ex vivo biodistributions were performed after PET and optical imaging (4 h after injection). Organs and tissues were collected, weighed, and γ-counted. The %ID/g was based on a standard containing 1% of the injected dose.

Statistical Analysis

Radiolabeling values are reported as mean ± SD. Ex vivo biodistribution data are shown as box-and-whiskers (minimum to maximum) plots, and values are reported as mean ± SEM. For statistical analysis, multiple *t* tests (Holm–Sidak method, with $\alpha = 0.05$) were performed (Prism 7; GraphPad Software, Inc.).

RESULTS

Synthesis of the DML

We designed and successfully synthesized a multifunctional linker (Fig. 1A) that contains functional groups for site-specific conjugation to engineered antibody fragments by thiol-reactive maleimide, incorporation of a fluorescent dye via amine-reactive NHS ester, and rapid and efficient radiolabeling by the reaction of 1,2,4,5-tetrazine with ^{18}F-TCO via the bioorthogonal IEDDA cycloaddition (click chemistry). Starting from α-boc-L-lysine, the synthesis was achieved in 2 steps. The purity was more than 95% as confirmed by high-performance liquid chromatography.

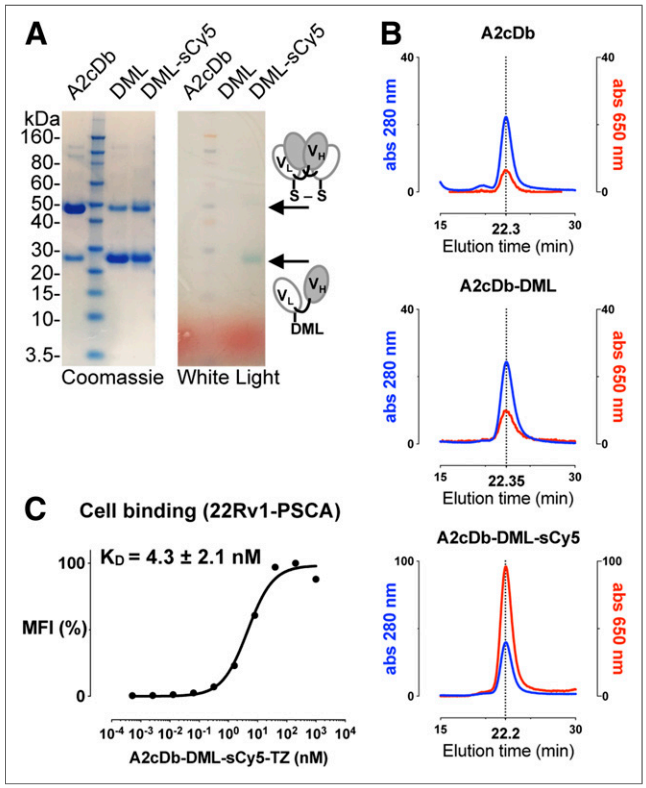

FIGURE 2. Biochemical characterization of DML-conjugated A2cDb. (A) Sodium dodecyl sulfate–polyacrylamide gel electrophoresis analysis of A2cDb and site-specifically conjugated A2cDb under nonreducing conditions: Coomassie-stained and unstained (white light). (B) Size exclusion chromatography of A2cDb, A2cDb-DML, and A2cDb-DML-sCy5 shows similar elution profiles for protein (280 nm). Fluorescent dye (sCy5, 650 nm) elutes at same time as protein (22.2 min), confirming conjugation to A2cDb. (C) Binding of A2cDb-DML-sCy5 to 22Rv1-PSCA cells analyzed by flow cytometry. Saturation binding curve of 1 of 3 independent experiments is shown. Apparent affinity of A2cDb-DML-sCy5 was calculated using single-site specific binding model. MFI = mean fluorescence intensity.

TABLE 1
Radiolabeling of A2cDb Using ^{18}F-TCO Click Chemistry

Parameter	^{18}F-DML-A2cDb		^{18}F-DMLsCy5-A2cDb	
	Mean	SD	Mean	SD
D/P ratio	ND		1.07	0.26
Labeling efficiency (%)	77.1	17.7	52.7	18.6
Specific activity (MBq/μg)	0.41	0.12	0.50	0.30
Radiochemical purity (%)	97.3	1.6	89.1	10.6
Immunoreactivity (%)	42.9	8.7	41.5	6.9
n	3		3	

ND = not determined.

Site-Specific Conjugation of the DML to A2cDb

The DML was deprotected and conjugated with sulfo-cyanine5 NHS ester (DMLsCy5, Fig. 1B) followed by conjugation to the reduced C-terminal cysteine residues of the anti-PSCA A2cDb (A2cDb-DML-sCy5) (Fig. 1C).

Successful conjugation of the DML or DML-sCy5 to A2cDb was confirmed by sodium dodecyl sulfate–polyacrylamide gel electrophoresis analysis (denaturing, nonreducing conditions). The unconjugated cDb predominantly exists as a covalent dimer migrating at 50 kDa (theoretic molecular weight, 50.6 kDa). With the C-terminal interchain disulfide bridge reduced and conjugated to DML or DML-sCy5, most of the protein migrates at about 25 kDa, corresponding to the molecular weight of the monomer. The blue sCy5 can be seen under white light concurrent with the monomer band of A2cDb-DMLsCy5 (Fig. 2A). Purity and integrity of the conjugated A2cDb (noncovalent dimer) were confirmed by size-exclusion chromatography (Fig. 2B). Both A2cDb-DML and A2cDb-DMLsCy5 eluted as single peaks at similar elution times as the unconjugated A2cDb (22.3 min), and A2cDb-DMLsCy5 showed a concurring peak for the fluorescent dye (650 nm). These results confirm that conjugation of the DML did not disrupt dimer formation of the cDb. Specific binding of A2cDb-DMLsCy5 to cell-surface–expressed antigen was verified by flow cytometry using the prostate cancer cell line 22Rv1 transduced to express PSCA (22Rv1-PSCA). The low nanomolar apparent affinity (K_D, 4.3 ± 2.1 nM; n = 3), as calculated from saturation binding curves, was unchanged compared with previously published data (*13,20*).

Radiofluorination of A2cDb-DML and A2cDb-DMLsCy5 using ^{18}F-TCO click chemistry was performed within 10 min at room temperature and resulted in comparable specific activities (Table 1). Labeling efficiencies varied depending on the amount of ^{18}F-TCO that could be added to the reaction (limited by the final dimethyl sulfoxide concentration of 10%). Radiochemical purity (after size-exclusion spin column) and immunoreactive fraction were comparable between ^{18}F-DML-A2cDb and ^{18}F-DMLsCy5-A2cDb.

Demonstration of PSCA-Specific Tumor Uptake Using Noninvasive Whole-Body ^{18}F-Immuno-PET Imaging

Single-modality ^{18}F-DML-A2cDb or dual-modality ^{18}F-DMLsCy5-A2cDb (10 μg/3–4.8 MBq) were injected intravenously into male nude mice bearing 22Rv1 (left shoulder) and 22Rv1-PSCA (right shoulder) xenografts (Fig. 3). Antigen-specific uptake of both tracers was seen in the PSCA-expressing tumor as early as 1 h after injection (Figs. 3A and 3C) and was retained over the 4-h imaging study (Figs. 3B and 3D). Minimal activity in the negative tumor, presumably caused by blood-pool activity, decreased over time. Clearance of ^{18}F-DML-A2cDb (Figs. 3A and 3B) appeared to be primarily renal, and activity was excreted into the urine (bladder). Some clearance occurred through the hepatobiliary route, and excretion of activity with the feces could be seen. The biodistribution of ^{18}F-DMLsCy5-A2cDb differed from that of single-modality ^{18}F-DML-A2cDb, with higher blood-pool activity at all time points (visible in the heart) and higher activity in both liver and kidneys (Figs. 3C and 3D). Importantly, the specificity of both tracers was retained, because PSCA-specific tumor uptake (22Rv1-PSCA) was higher than 22Rv1, and despite the differing biodistributions, uptake in 22Rv1-PSCA was similar for both tracers over 4 h.

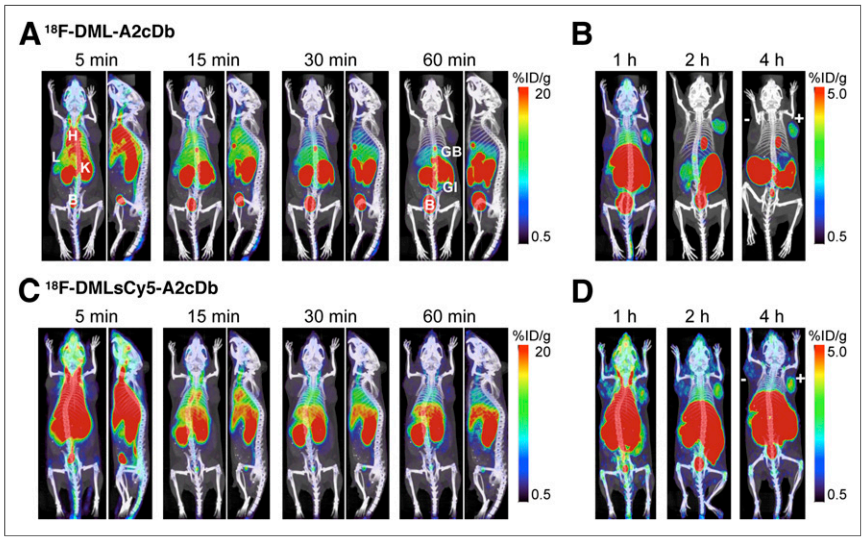

FIGURE 3. Immuno-PET imaging shows antigen-specific uptake in PSCA-positive prostate cancer xenografts. Nude mice bearing PSCA-negative (22Rv1, left shoulder) and PSCA-positive (22Rv1-PSCA, right shoulder) subcutaneous xenografts were imaged with single-modality ^{18}F-DML-A2cDb 60-min dynamic scan (A) and 10-min static scans at 1, 2, and 4 h after injection (B) or dual-modality ^{18}F-DMLsCy5-A2cDb 60-min dynamic scan (C) and 10-min static scans at 1, 2, and 4 h after injection (D). Depicted are representative scans (of $n \geq 6$) as whole-body maximum-intensity-projection small-animal PET/CT overlays.

Identification of PSCA-Positive Tumor Tissue Using Intraoperative Fluorescent Imaging

After the last PET/CT scan (4 h after injection), optical imaging of the same mice was performed postmortem with the skin removed (mimicking a surgical setting) using the IVIS Lumina II system. Fluorescent signal was detected in the PSCA-positive xenografts of mice injected with ^{18}F-DMLsCy5-A2cDb (Fig. 4A). Signal intensity was higher in 22Rv1-PSCA tumors (right shoulder) than in 22Rv1 tumors (left shoulder) and surrounding tissue. Tumors were further

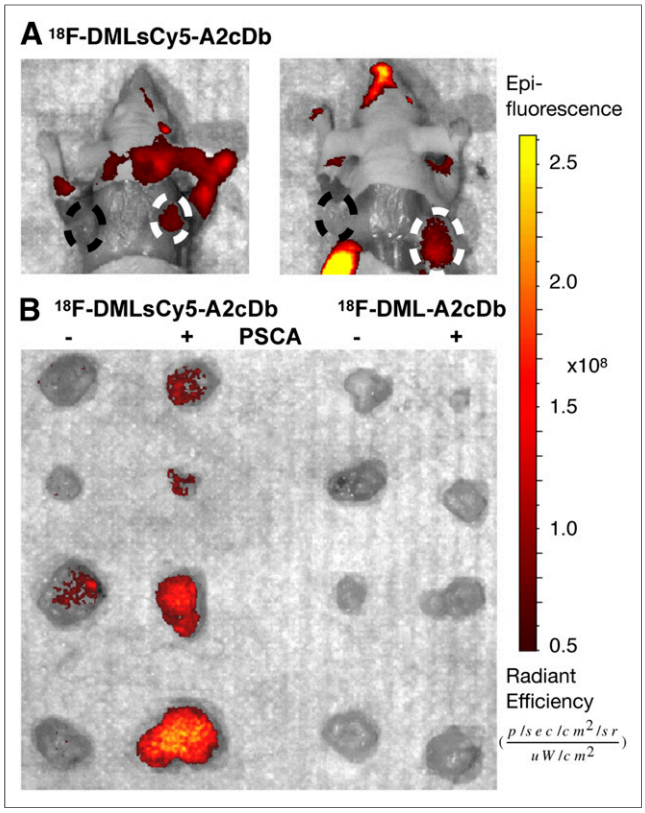

FIGURE 4. Same mice were assessed by optical imaging. (A) Postmortem optical imaging of mice with skin removed. Mice injected with dual-modality ^{18}F-DMLsCy5-A2cDb show antigen-specific fluorescence signal in PSCA-positive tumor on right shoulder (dashed circle). Two representative mice (of $n = 7$) are shown. (B) 22Rv1 (−) and 22Rv1-PSCA (+) xenografts were analyzed ex vivo to compare relative fluorescent signal without obstruction from other organs.

analyzed ex vivo to compare the relative fluorescent signals without interference from other organs or autofluorescence from the skin (Fig. 4B). Although ^{18}F-DMLsCy5-A2cDb clearly distinguished PSCA-positive from -negative tumors, no signal was detected in tumors from the ^{18}F-DML-A2cDb group. Fluorescence imaging of excised organs and tissues showed expected autofluorescence in the stomach, intestine, and to a lesser extent kidneys of mice injected with ^{18}F-DML-A2cDb (Supplemental Fig. 1). In the ^{18}F-DMLsCy5-A2cDb group, a higher fluorescent signal was detected in the organs of clearance—liver, gallbladder, spleen, and kidneys—consistent with the immuno-PET images.

Quantitative ROI Analysis and Ex Vivo Biodistribution

Quantitative ROI analysis of ^{18}F-DML-A2cDb immuno-PET showed rapid blood clearance, renal clearance and excretion, and antigen-specific retention of the tracer in the tumor (22Rv1-PSCA). ^{18}F-DMLsCy5-A2cDb immuno-PET revealed a larger fraction of the tracer clearing through the liver and a slower decrease of activity in the kidneys (Fig. 5A).

Ex vivo biodistributions (4 h after injection; Fig. 5B; Table 2) confirmed that uptake in PSCA-expressing tumors was similar for ^{18}F-DML-A2cDb and the dual-modality ^{18}F-DMLsCy5-A2cDb (2.8 ± 1.1 and 2.9 ± 0.4 %ID/g, respectively) and was significantly higher than in 22Rv1 tumors (0.3 ± 0.1 and 0.8 ± 0.2 %ID/g, respectively; $P < 0.05$ for both). The longer retention of ^{18}F-DMLsCy5-A2cDb radioactive signal seen in the immuno-PET scans was consistent with the higher remaining activity in the liver (4.8 ± 0.3 %ID/g), kidneys (15.2 ± 1.1 %ID/g), and spleen (2.2 ± 0.2 %ID/g). In contrast, ^{18}F-DML-A2cDb showed the highest activity excreted in the intestine at 4 h after injection (13.7 ± 2.7 %ID/g, including contents).

DISCUSSION

Immuno-PET imaging could improve diagnosis and surgical planning, and fluorescence image–guided surgery could enable more complete resection of diseased tissues in cancer patients who stand to benefit from surgery (e.g., pancreatic and prostate cancer). Combining both signaling moieties into a single agent guarantees direct correlation between the diagnostic imaging for surgical planning and the imaging used to direct surgery (*1*).

Although the combination of PET and fluorescence imaging has been extensively studied, most approaches have used intact antibodies and random conjugation methods that result in a Poisson distribution of number of D/P fractions with distinct pharmacokinetic characteristics (affinity, clearance and distribution, fluorescence quenching, and residualizing of metabolites) (*26*). Smaller antibody fragments exhibit optimized pharmacokinetics for imaging (better tumor penetration and faster clearance) and can be combined with shorter-lived radionuclides to reduce the radiation dose to healthy tissues (compared with traditional immuno-PET with IgGs and long-lived isotopes). However, because of their smaller size, antibody fragments are all the more prone to undergo changes in tissue retention and blood clearance on modification with radionuclides, chelators, or fluorescent dyes (depending on site, shape, size, hydrophobicity, and charge) (*27*). Thus, controlling the location and stoichiometry of modifications is critical.

We generated a universal multifunctional linker (DML) that allows consistent conjugation with a known number of linkers per protein and to defined sites, thereby minimizing batch-to-batch heterogeneity and guaranteeing more predictable properties. Most importantly, 2 imaging moieties can be added to the protein with a single modification.

The DML was successfully labeled with sCy5 and site-specifically conjugated to the anti-PSCA A2cDb (A2cDb-DMLsCy5) and did not impair the dimeric conformation or binding characteristics of A2cDb. Radiofluorination was conducted using click chemistry within 10 min (^{18}F-DMLsCy5-A2cDb), and in vivo specificity was shown for both modalities by successive PET and fluorescence imaging of mice bearing PSCA-positive and -negative xenografts. ^{18}F-immuno-PET showed fast and specific tumor uptake and rapid clearance from circulation, resulting in high-contrast images as early as 1 h after injection. Postmortem optical imaging confirmed high-contrast fluorescence in the PSCA-expressing tumors and excellent delineation of cancerous cells from surrounding tissue.

The exceptional speed of the IEDDA reaction facilitates the use of ^{18}F (half-life, 109.8 min), which well matches the biologic half-life of the diabody format. Williams et al. compared different-sized derivatives of the same full-length IgG (scFv, diabody, minibody, $F(ab')_2$, IgG) with respect to affinity (K_D) and imaging figure of merit, an indicator of how rapidly a statistically significant tumor image can be acquired (*28,29*). The analysis suggested that same-day imaging would be best accomplished with the diabody format (3- to 5-h interval after injection) and that if the imaging figure of merit was calculated for ^{18}F, only the diabody was competitive, as the larger-sized fragments have half-lives that are too long and the smaller monovalent scFv showed much shorter tumor retention. The in vivo results using ^{18}F-DMLsCy5-A2cDb presented in this work

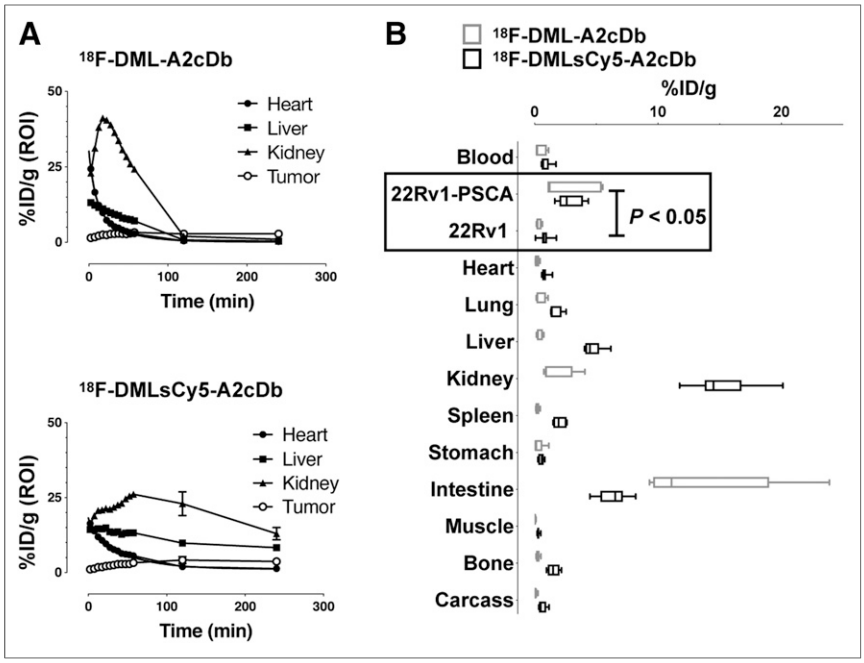

FIGURE 5. Quantitative ROI analysis and ex vivo biodistribution. (A) Quantitative ROI analysis of blood (heart), liver, kidney, and 22Rv1-PSCA tumor. (B) Ex vivo biodistribution 4 h after injection of ^{18}F-DML-A2cDb (n = 6) and ^{18}F-DMLsCy5-A2cDb (n = 7). Tumors and organs were harvested and γ-counted.

indeed show that same-day immuno-PET imaging is feasible and further corroborate previous studies with ^{18}F-labeled diabodies in several models (human epidermal growth factor receptor 2, carcinoembryonic antigen, CD20) (*29–31*).

While radioactive decay happens only once, the fluorescent dye can provide greater sensitivity for intraoperative guidance because it can repeatedly be activated by excitation light. The long intracellular (lysosomal) half-life of sCy5 (half-life, 3.9 ± 0.5 d) further extends the possible time window between presurgical whole-body immuno-PET and fluorescence image–guided surgery (*15*).

The fluorescent dye sCy5 was chosen for this study over the previously used IRDye800CW because we hypothesized that the former would have less impact on the pharmacokinetic properties of the A2cDb because of its smaller size, lower charge, and lower hydrophobicity. Although the antigen-specific tumor uptake was similar between ^{18}F-DML-A2cDb and ^{18}F-DMLsCy5-A2cDb, significant differences were observed in clearance of the dual-modality tracer, with longer retention in liver, spleen, and kidneys. This finding could be due to the relatively high D/P ratio of 1.1 ± 0.3, since a study by Cilliers et al. suggested that D/P ratios of 0.3 or less are necessary to limit the impact of fluorophores on antibody pharmacokinetics after comparing 2 IgGs (trastuzumab and bevacizumab) labeled non–site-specifically with either IRDye800CW or Alexa Fluor 680 at different D/P ratios (*26*).

Because of the modular linker system, the fluorophore can easily be exchanged if desired, and because the linker-to-protein ratio is precisely controlled, the D/P ratio can also be tailored, such as by mixing DML and DML-sCy5. Future studies will have to evaluate the dual-modality tracer ^{18}F-DMLsCy5-A2cDb with an optimized D/P ratio in more relevant preclinical cancer models (orthotopic tumors or transgenic mice) to assess sufficient contrast with surrounding tissues and the impact of tissue autofluorescence in the far-red light range. Another consideration is that normal tissue expression of PSCA in prostate, bladder, and stomach is not reflected in the xenograft model because the A2cDb does not cross-react with murine PSCA.

A limitation of the radiolabeling procedure was the low concentration of ^{18}F; this strained the kinetics in the labeling reaction because of the maximum amount of organic solvent to which the protein can be exposed. However, future optimization of the radiosynthesis, purification, and elution procedures should lead to higher a ^{18}F-TCO concentration or specific activity and thus higher labeling efficiencies.

The high clinical relevance of targeted dual-modality probes for prostate cancer is reflected by the variety of ongoing preclinical studies exploring, for example, prostate-specific membrane antigen inhibitors, monoclonal antibodies, or gastrin-releasing peptide receptor ligands for dual-modality imaging (*5,32,33*). Site-specific conjugation to engineered cysteine residues is well established, and the DML could be broadly applied to antibody fragments, single-domain antibodies, or alternative scaffolds targeting cell-surface markers for molecular imaging with any combination of dual-modality PET/fluorescence. Alternative targeting moieties and tumor markers should be explored in future studies to confirm the universal applicability of the DML. The precision and speed of the IEDDA reaction have also been shown to be feasible in vivo, and the DML could be used for pretargeted imaging strategies (*34,35*).

TABLE 2
Ex Vivo Biodistribution 4 Hours After Injection

Site	^{18}F-DML-A2cDb		^{18}F-DMLsCy5-A2cDb	
	Mean	SEM	Mean	SEM
Blood	0.44	0.19	0.90	0.17
22Rv1-PSCA (+)	2.84	1.07	2.89	0.38
22Rv1 (−)	0.32	0.09	0.82	0.19
Heart	0.18	0.07	0.85	0.11
Lung	0.44	0.17	1.67	0.19
Liver	0.37	0.10	4.81	0.29
Kidney	1.71	0.56	15.2	1.1
Spleen	0.21	0.06	2.02	0.17
Stomach	0.31	0.10	0.54	0.08
Intestine	13.7	2.7	6.37	0.46
Muscle	0.05	0.01	0.30	0.04
Bone	0.25	0.06	1.53	0.17
Carcass	0.11	0.04	0.66	0.13
n	6		7	

Data are %ID/g mean ± SE of mean.

CONCLUSION

This study presents a universal DML for site-specific conjugation to antibody fragments via engineered cysteine residues. This linker enables stoichiometric conjugation of near-infrared fluorescent dyes away from the antigen binding site and the use of rapid and efficient click chemistry for radiolabeling with ^{18}F. Dual-modality imaging could provide both noninvasive whole-body imaging to localize PSCA-positive cancer and fluorescence image–guided identification of tumor margins and lymphatic spread.

DISCLOSURE

This work was supported by NIH R01 CA174294, the UCLA SPORE in Prostate Cancer (NIH P50 CA092131), Department of Defense Synergistic IDEA Award W81XWH-15-1-0725, and a generous gift from Ralph and Marjorie Crump to the Crump Institute. Small-animal imaging was funded in part by a UCLA Jonsson Comprehensive Cancer Center (JCCC) support grant (NIH CA016042). Anna Wu is a member of the JCCC and holds ownership interest in and is a consultant/advisory board member for ImaginAb, Inc. No other potential conflict of interest relevant to this article was reported.

ACKNOWLEDGMENTS

We thank the staff of the UCLA Biomedical Cyclotron and Dr. Umesh Gangadharmath for providing ^{18}F-fluoride for our study. We thank Felix B. Salazar for technical assistance and the UCLA Crump Preclinical Imaging Technology Center for help with small-animal imaging.

KEY POINTS

QUESTION: Can antibody fragments be site-specifically conjugated for immuno-PET and fluorescence imaging using a novel DML?

PERTINENT FINDINGS: To generate a dual-modality antibody-based imaging agent, the DML was labeled with sCy5, site-specifically conjugated to the C-terminal cysteine of A2cDb, and subsequently radiolabeled by click chemistry with ^{18}F-TCO. The new imaging probe (^{18}F-DMLsCy5-A2cDb) was evaluated in a human PSCA-positive prostate cancer xenograft model by sequential immuno-PET and optical imaging and showed antigen-specific uptake in PSCA-expressing tumors.

IMPLICATIONS FOR PATIENT CARE: The humanized antibody fragment could be translated into the clinic and provide both noninvasive whole-body PET imaging to localize PSCA-positive cancer and fluorescence image–guided identification of tumor margins during surgery.

REFERENCES

1. Azhdarinia A, Ghosh P, Ghosh S, Wilganowski N, Sevick-Muraca EM. Dual-labeling strategies for nuclear and fluorescence molecular imaging: a review and analysis. *Mol Imaging Biol.* 2012;14:261–276.
2. Bond-Smith G, Banga N, Hammond TM, Imber CJ. Pancreatic adenocarcinoma. *BMJ.* 2012;344:e2476.
3. Heidenreich A, Bastian PJ, Bellmunt J, et al. EAU guidelines on prostate cancer. Part 1: screening, diagnosis, and local treatment with curative intent—update 2013. *Eur Urol.* 2014;65:124–137.
4. Lee S, Chen X. Dual-modality probes for in vivo molecular imaging. *Mol Imaging.* 2009;8:87–100.
5. Lütje S, Rijpkema M, Franssen GM, et al. Dual-modality image-guided surgery of prostate cancer with a radiolabeled fluorescent anti-PSMA monoclonal antibody. *J Nucl Med.* 2014;55:995–1001.
6. Olafsen T, Wu AM. Antibody vectors for imaging. *Semin Nucl Med.* 2010;40:167–181.
7. Olafsen T, Cheung CW, Yazaki PJ, et al. Covalent disulfide-linked anti-CEA diabody allows site-specific conjugation and radiolabeling for tumor targeting applications. *Protein Eng Des Sel.* 2004;17:21–27.
8. Adumeau P, Sharma SK, Brent C, Zeglis BM. Site-specifically labeled immunoconjugates for molecular imaging—part 1: cysteine residues and glycans. *Mol Imaging Biol.* 2016;18:1–17.
9. Gioux S, Choi HS, Frangioni JV. Image-guided surgery using invisible near-infrared light: fundamentals of clinical translation. *Mol Imaging.* 2010;9:237–255.
10. Vahrmeijer AL, Hutteman M, van der Vorst JR, van de Velde CJ, Frangioni JV. Image-guided cancer surgery using near-infrared fluorescence. *Nat Rev Clin Oncol.* 2013;10:507–518.
11. Te Velde EA, Veerman T, Subramaniam V, Ruers T. The use of fluorescent dyes and probes in surgical oncology. *Eur J Surg Oncol.* 2010;36:6–15.
12. Tsai WK, Zettlitz KA, Tavare R, Kobayashi N, Reiter RE, Wu AM. Dual-modality immunoPET/fluorescence imaging of prostate cancer with an anti-PSCA cys-minibody. *Theranostics.* 2018;8:5903–5914.
13. Zettlitz KA, Tsai WK, Knowles SM, et al. Dual-modality immuno-PET and near-infrared fluorescence imaging of pancreatic cancer using an anti-prostate stem cell antigen cys-diabody. *J Nucl Med.* 2018;59:1398–1405.
14. Hughes LD, Rawle RJ, Boxer SG. Choose your label wisely: water-soluble fluorophores often interact with lipid bilayers. *PLoS One.* 2014;9:e87649.
15. Cilliers C, Liao J, Atangcho L, Thurber GM. Residualization rates of near-infrared dyes for the rational design of molecular imaging agents. *Mol Imaging Biol.* 2015;17:757–762.
16. Lang K, Chin JW. Bioorthogonal reactions for labeling proteins. *ACS Chem Biol.* 2014;9:16–20.
17. Li Z, Cai H, Hassink M, et al. Tetrazine-trans-cyclooctene ligation for the rapid construction of ^{18}F labeled probes. *Chem Commun (Camb).* 2010;46:8043–8045.
18. Reiner T, Zeglis BM. The inverse electron demand Diels-Alder click reaction in radiochemistry. *J Labelled Comp Radiopharm.* 2014;57:285–290.
19. Lepin EJ, Leyton JV, Zhou Y, et al. An affinity matured minibody for PET imaging of prostate stem cell antigen (PSCA)-expressing tumors. *Eur J Nucl Med Mol Imaging.* 2010;37:1529–1538.
20. Sonn GA, Behesnilian AS, Jiang ZK, et al. Fluorescent image-guided surgery with an anti-prostate stem cell antigen (PSCA) diabody enables targeted resection of mouse prostate cancer xenografts in real time. *Clin Cancer Res.* 2016;22:1403–1412.
21. Saffran DC, Raitano AB, Hubert RS, Witte ON, Reiter RE, Jakobovits A. Anti-PSCA mAbs inhibit tumor growth and metastasis formation and prolong the survival of mice bearing human prostate cancer xenografts. *Proc Natl Acad Sci USA.* 2001;98:2658–2663.
22. Collins J, Waldmann CM, Drake C, et al. Production of diverse PET probes with limited resources: 24 ^{18}F-labeled compounds prepared with a single radiosynthesizer. *Proc Natl Acad Sci USA.* 2017;114:11309–11314.
23. Molander GA, Shin I. Synthesis and Suzuki-Miyaura cross-coupling reactions of potassium Boc-protected aminomethyltrifluoroborate with aryl and hetaryl halides. *Org Lett.* 2011;13:3956–3959.
24. Yang J, Karver MR, Li W, Sahu S, Devaraj NK. Metal-catalyzed one-pot synthesis of tetrazines directly from aliphatic nitriles and hydrazine. *Angew Chem Int Ed Engl.* 2012;51:5222–5225.
25. Loening AM, Gambhir SS. AMIDE: a free software tool for multimodality medical image analysis. *Mol Imaging.* 2003;2:131–137.
26. Cilliers C, Nessler I, Christodolu N, Thurber GM. Tracking antibody distribution with near-infrared fluorescent dyes: impact of dye structure and degree of labeling on plasma clearance. *Mol Pharm.* 2017;14:1623–1633.
27. Boswell CA, Tesar DB, Mukhyala K, Theil FP, Fielder PJ, Khawli LA. Effects of charge on antibody tissue distribution and pharmacokinetics. *Bioconjug Chem.* 2010;21:2153–2163.
28. Williams LE, Wu AM, Yazaki PJ, et al. Numerical selection of optimal tumor imaging agents with application to engineered antibodies. *Cancer Biother Radiopharm.* 2001;16:25–35.
29. Cai W, Olafsen T, Zhang X, et al. PET imaging of colorectal cancer in xenograft-bearing mice by use of an ^{18}F-labeled T84.66 anti-carcinoembryonic antigen diabody. *J Nucl Med.* 2007;48:304–310.
30. Olafsen T, Sirk SJ, Olma S, Shen CK, Wu AM. ImmunoPET using engineered antibody fragments: fluorine-18 labeled diabodies for same-day imaging. *Tumour Biol.* 2012;33:669–677.
31. Zettlitz KA, Tavare R, Collins J, et al. ^{18}F-labeled anti-human CD20 cys-diabody for same-day immunoPET in a model of aggressive B-cell lymphoma in human CD20 transgenic mice. *Eur J Nucl Med Mol Imaging.* 2019;46:489–500.
32. Baranski AC, Schafer M, Bauder-Wust U, et al. PSMA-11-derived dual-labeled PSMA inhibitors for preoperative PET imaging and precise fluorescence-guided surgery of prostate cancer. *J Nucl Med.* 2018;59:639–645.
33. Zhang H, Desai P, Koike Y, et al. Dual-modality imaging of prostate cancer with a fluorescent and radiogallium-labeled gastrin-releasing peptide receptor antagonist. *J Nucl Med.* 2017;58:29–35.
34. Denk C, Svatunek D, Filip T, et al. Development of a ^{18}F-labeled tetrazine with favorable pharmacokinetics for bioorthogonal PET imaging. *Angew Chem Int Ed Engl.* 2014;53:9655–9659.
35. Devaraj NK, Weissleder R. Biomedical applications of tetrazine cycloadditions. *Acc Chem Res.* 2011;44:816–827.